ELSEVIER

Contents lists available at ScienceDirect

Journal of Materials Processing Tech.

journal homepage: www.elsevier.com/locate/jmatprotec





Ultrasonic elastography for nondestructive evaluation of dissimilar material joints

Yuqi Jin^{a,b,1}, Tianhao Wang^{c,d,1}, Arkadii Krokhin^a, Tae-Youl Choi^b, Rajiv S. Mishra^c, Arup Neogi^{a, *}

- ^a Department of Physics, University of North Texas, Denton, P.O. Box 311427, Denton, TX, 76203, USA
- b Department of Mechanica Engineering, University of North Texas, 3940 North Elm Street, Suite F101, Denton, TX, 76207, USA
- ^c Department of Material Science and Engineering, University of North Texas, 3940 North Elm Street, Suite E132, Denton, TX, 76207, USA
- d Energy and Environment Directorate, Pacific Northwest National Laboratory, 902 Battelle Blvd., Richland, WA, 99352, USA

ARTICLE INFO

Associate Editor: Hui-Ping Wang

Keywords:
Friction stir processing
Non-destructive evaluation
Elastography
Mechanical properties of metals
Friction stir welding
Elastic modulus
Ultrasonic inspection

ABSTRACT

Dissimilar material joints or multilayered metals have become inevitable in the manufacturing industry due to the increasing demand for multifunctional materials with variable mechanical, thermal, or electrical characteristics in a single assembly. Lattice mismatch of materials at the interface of dissimilar materials leads to inferior mechanical characteristics. In particular, the mismatch in elastic properties indicated by a large initial elastic deformation is critical to determine the extent of variation in stress. However, nanoindentation, the most common and accepted technique to measure elastic modulus, is destructive, time-consuming, and can only examine mechanical properties within a limited area. A non-invasive elastographic mapping technique evaluates the mechanical properties using ultrasonic elastography to study incompressibility. The dissimilar joint between steel and copper was obtained via friction stir welding. The variation of the stress developed at the welded joint of the two different metals was evaluated from the dynamic bulk modulus map. A tensile test of the involved workpiece confirmed a good agreement with our analysis based on the dynamic bulk modulus elastographic mapping results. This study provides a rapid and non-invasive technique for the bulk metallurgic elastic modulus inspection to overcome the limitations of conventional methods.

1. Introduction

Joints of materials with different physical characteristics are increasingly integrated into a single block to realize multifunctional physical characteristics for meeting modern manufacturing industries' demands[1]. Metals with various thermal, electrical, or mechanical properties can be combined with different manufacturing techniques to realize a new hybrid material system. Automotive and aerospace industries require single blocks of lightweight materials and high-strength materials for enhanced energy efficiency without compromising the designed structures' mechanical strength[1]. Various high-efficiency manufacturing techniques can achieve that, including additive manufacturing, or welding methods for joining dissimilar materials such as laser welding of steel/Copper/Aluminum combinations by Mai and Spowage (2004) and friction stir welding (FSW) of variance materials summarized by DebRoy and Bhadeshia (2010). However, the differences

in the melting points of various materials make it challenging to use a melting-based welding process to achieve joints with high mechanical strengths. Friction stir welding has better adaptability for joining dissimilar materials than laser welding since FSW is a solid-state welding method without melting constituent components. During the FSW process, a rotating tool consisting of a shoulder and a probe affects two workpieces' adjoining interface (base materials) due to the heat-induced by friction at the joint. Thomas et al. (1991) found that in order to stir the plastically deformed workpieces into a single joint, frictional heating typically raises temperatures beyond the softening transition point, but below the melting point, of the workpieces. Thomas et al. (1999) reported the influx of less heat into the base materials during the welding process serves as a significant advantage of FSW compared with most conventional fusion-based welding techniques since unexpected heat-induced elastic modulus variation in the final product can be significantly reduced in steel system, which was also verified by Lienert

E-mail address: arupn@yahoo.com (A. Neogi).

 $^{^{\}star}$ Corresponding author.

¹ Equal Contribution first authors.

et al. (2003). Peng et al. (2003) concluded this variation of the temperature-induced elastic deformation can result in cracks or failures that are commonly initiated and propagate around the welded interface due to the non-equilibrium process and non-uniform stress or thermal gradient induced by the solid state welding processes such as ultrasonic welding and friction welding studied by Tsujino et al. (2002) and Taban et al. (2010), including FSW processes reported by Coelho et al. (2008) and Uzun et al. (2005). Xue et al. (2011) observsed and concluded that flaws at the joint are due to the formation of the intermetallic compound (IMC) layer and (or) oxide layer when the base materials were metallurgically miscible. Tanaka et al. (2009) verified the impact of IMC formation by proforming mechanical tests. The cracks are rapidly initiated at the joint and can propagate due to the low ductility and weak bonding at the interface between the IMC layer and (or) oxide layer parent materials. Recently, Wang and Mishra (2019) showed that a crack initiated at a welding interface between dissimilar workpieces could be correlated with elastic modulus mismatch and resultant stress concentration under mechanical loading in immersible material combinations. Therefore, the variation of elastic modulus across the dissimilar material joint is critical to qualify and predict joint strength and reliability. In this work, we present a nondestructive ultrasonic elastography technique to evaluate the mechanical strength of dissimilar joints by characterizing the effective bulk modulus of the materials at

In many welding workpieces inspections, phased array transducers are commonly used for the echo-intensity or time-of-flight mapping to locate the discontinuities normally referred to flaw and defects. Lévesque et al. (2016) demenstrated the clear exiamination of a welding joint discontinuity map using phased array acoustic system. Shiraishi et al. (2010) used higher operating frequency photoacoustic measurements for high-resolution flaw detection. These instant-evaluation techniques focus solely on the discontinuities around the welded interface instead of evaluating local elastic parameters. Furthermore, some in-situ methods were also invented and studied for internal or surface flaw controlling by monitoring thermal gradient field showed by Venkatakrishna et al. (2020) and surface profile using electromagnetic and acoustic techniques reported by Hartl et al. (2019) and Sudhagar et al. (2019). The complexity of friction stir welding with the multi-parameter interference during the processing is high even in mono-material system. Mishra et al. (2020) applied machine learning to study and analyze the welding parameters to automatically select suitable conditions for the works showing nice performance from the quality of the products. Du et al. (2019) and Du et al. (2020) also pointed out the influence on products quality affected by tool condition and machine feedback information which were also able to be studied and predicted by machine learning programs. With the AI selected parameters, the flaw in the welding path was minimized. Although mechanical discontinuities serve as a significant indicator of the presence of macroscopic defects, more precise and qualitative techniques are necessary for the evaluation of local elastic and plastic characteristics of welding workpieces.

Three major elastic constants characterize mechanical deformation/ elongation resistance to different type of stress in linear elasticity. Young's modulus (E) indicates strain resistance under tensile or compress stress; bulk modulus (K) is the volumetric strain resistant of the material under volumetric compression or tensile stress; Poisson's ratio (σ) shows the ratio of the transverse compression to the longitudinal extension. They are related by the formula $K = E/3(1-2\sigma)$.

In the conventional techniques, tensile testing and nanoindentation applied by Wu et al. (2010) are the two most commonly applied destructive elastic and plastic property testing methods. The site-specific mini-tensile test technique does provide an accurate estimate of the elastic modulus. Nano-indentation is a standard method for characterizing the effective Young's modulus using Young's modulus and Poisson ratio of the indenter head material and an assumption of sample Poisson's ratio. These techniques are limited by time-consuming sample preparation and sample evaluation size compared to the workpiece's

actual size.

Besides the destructive elasticity evaluation, Zuev et al. (1999) has demenstrated conventional ultrasonic elastic modulus testing as a non-destructive technique requires longitudinal and transverse modes of ultrasound to calculate elastic modulus or flaws by physical contact with the specimen. The method is broadly applied and provided a lot of valuable information for both academia and industries, and recently still active as the work from He et al. (2020) reported. The need for physical contact between the transducer and the sample surface limits measurement accuracy, especially in welded products, as the sample surface is generally rough without any additional post-processing. A liquid coupling material can be used to avoid direct contact between the transducer facet with a rough sample surface. However, using a liquid ambient invalidates the estimation of transverse modulus, such as Young's modulus and shear modulus, due to a lack of propagating transverse mode in fluids. In this study, the recently invented by Jin et al. (2019) named Effective density and dynamic Bulk Modulus Elastography (EBME) was utilized to evaluate a welding joint's quality between two dissimilar materials mapping elastic modulus distribution without direct contacting. Jin et al. (2020b) and Jin et al. (2020c) has applied the EBME method on additive manufacturing products for estimating the dynamic bulk modulus and effective density which showed exceptional results well agreed with the characterizations from conventional techniques.

A Copper (Cu) - 316 stainless steel (SS316) joint via FSW was selected for investigation as Cu and Fe are metallurgically immiscible, making the influence of IMC excludable. Wang et al. (2018) reported local mechanical mixing between Cu and Fe at the welded interface introduced via FSW facilitated robust bonding between the base materials. Furthermore, bonding between copper and stainless steel is extensively used in the nuclear industry, chemical, and automobile sectors as Akella et al. (2014) and Yao et al. (2009) mentioned.

Though EBME is a non-contact and non-destructive method, the dynamic bulk modulus determined from the technique has been shown to accurately characterize the bulk modulus compared with standard measurement methods in the acoustic non-dispersion media. The technique has a high resolution of determining the dynamic bulk modulus from experiments. The ease of use of EBME, combined with its ability to evaluate large areas, makes it desirable to assessing highly complex distributions of elasticity in both organic and inorganic materials systems as Heo et al. (2021) and Pantawane et al. (2021) demenstrated. The dynamic bulk modulus of a sample represents a coefficient in the linear response of the elastic medium to small oscillating deformation due to a longitudinal monochromatic wave propagating along the sample's cross-section. The static bulk modulus is usually examined from a low strain rate mechanical test. When the rate of change of strain to the deforming force is slow, the estimated value of elasticity is close to the traditionally defined elastic modulus, thereby serving as a measure of atomic forces. In the dynamic elasticity, the mechanical response may vary from the static response due to dispersion and scattering at grain boundaries and other inhomogeneities such as defects. The samples in our study are inhomogeneous in general. However, the internal zones and grains are much smaller than the operating wavelength. Therefore, the scanning occurs in the long-wavelength limit when the sample behaves like a homogeneous medium. Due to the relatively low frequency of the transducers used in this study, the macroscopic variation of the material's dynamic bulk modulus along the entire thickness of the metal joint can be measured. Nano-indentation or other destructive techniques generally measure the value of static modulus near the sample surface.

The dynamic bulk modulus (K) was calculated as described in our previous work Jin et al. (2019) and demonstrated in Fig. 1(D):

$$K = c Z_0 \left(\frac{-1 - \frac{p_1}{p_e - p_0} - \sqrt{4 \frac{p_1}{p_e - p_0} + 1}}{\frac{p_1}{p_e - p_0} - 2} \right), \quad \frac{Z}{Z_0} > 1$$
 (1)

where p_e is the maximum absolute magnitude of the emitted pulse from the transducer, p_0 and p_1 are the maximum absolute magnitude of reflection from the front and back surface of the sample, t_f and t_i are the start point and endpoint of the pulse, which determined from an automatic algorithm, c is the speed of sound in the sample, which is defined as $c = 2d/(t_f - t_i)$, Z is the acoustic impedance of the scanned sample, d is the thickness of the sample, and Z_0 is the reference acoustic impedance of the ambient material (deionized water in this study).

2. Experimental methods

FSW was carried out on an MTI RM-1 friction stir welding system (Fig. 1(A)). The critical welding parameters are as follows: Rotation rate. 400 RPM, traverse speed, 25 mm/min, plunge depth, 4.75 mm, tool tilt angle, 2°, and tool offset in copper, 2 mm. A W-Re tool was used for FSW. The tool dimensions are as follows: shoulder diameter, 16.0 mm, conical tool pin diameters, 5.0 mm at the tip and 7.0 mm at the bottom, and pin length, 4.0 mm. The tensile testing sample and cross-section of friction stir welded samples were cut by electrical discharge machining. Standard tensile tests of welded joints were conducted based on ASTM E8-04, and the cross-section sample was polished down to a surface finish till 0.02 µm diamond suspension. A cross-section of the sample was observed by optical microscopy and scanning electron microscopy (SEM) on FEI Nova NanoSEM 230 with a 15 kV accelerating voltage provided illustration Figure as Fig. 1E. Two-dimensional (2D) digital image correlation (DIC) was applied for localized deformation measurements during tensile testing. Before testing, the transverse sections of the welded specimens were painted by a random black speckle pattern over a white-painted surface. During testing, those black speckles were traced by a high-speed camera to measure the local strain. Microhardness was conducted on the cross-section of welded joints with a load of 200 g and a dwell time of 10 s which has been fabricated other samples previously in Wang (2018). The chemical composition of the base materials is:

Copper 110-99.9 % Copper, and 0.04 % Oxygen. Stainless steel 316-66 % Iron, 0.08 % Carbon, 2 % Manganese, 0.045 % Phosphorus, 0.03 % Sulfur, 0.75 % Silicon, 17 % Chromium, 12 % Nickel, 2 % Molybdenum, and 0.05 % Nitrogen.

The EBME scan had been performed before the tensile test and even before the sample was cut to conduct the tensile test.

In Fig. 1(B), a single Olympus Panametrics V301 1", 0.5 MHz plane wave immersion transducer operating at 0.5 MHz, was used for EBME. Scanning was achieved using a pulse-echo arrangement facilitated by a JSR Ultrasonics DPR 300 Pulser/Receiver. Pulses were emitted into the samples' smooth surface, and backscattered data was collected with a Tektronix MDO 3024b. Scanning was accomplished by translating the sample into 2-dimensions using a Newport UE41PP stepper motor controlled by an ESP 300Universal Motion Controller/Driver. A preprogrammed MATLAB code automated raster scanning motion and data acquisition. The ultrasound transducer and the scanned area of the sample were fully immersed in deionized water (DI) ambient at room temperature for more accurate and efficient pulse emission and echo detection. The total scanned area of the Cu-SS316 sample (Fig. 1(C)) was 10 mm on the welding axis by 35 mm on the lateral axis at 1 mm intervals. In the data acquisition, the time window has a fixed duration of 100 µs in every location. The recorded temporal signal is obtained on each scanned point due to averaging 512 signals recorded within the same time window in the oscilloscope. The whole experiment of EMBE took 2 hrs from setup to finish.

The values of the dynamic bulk modulus obtained from EBME measurement in water ambient depend on the deionized water quality. To increase accuracy of our results the impedance of water Z_0 was obtained by measuring the speed of sound and density before performing each EBME scan. The calibrated Z_0 value serves as input in Eq. (1).

The planar transducer generates an acoustic beam with 10 mm full width at half maximum (FWHM), and its near-field extends up to 54 mm. The tested sample was scanned with many narrow steps of 0.5 mm long. This transducer has demonstrated 1 GPa resolution in the previous

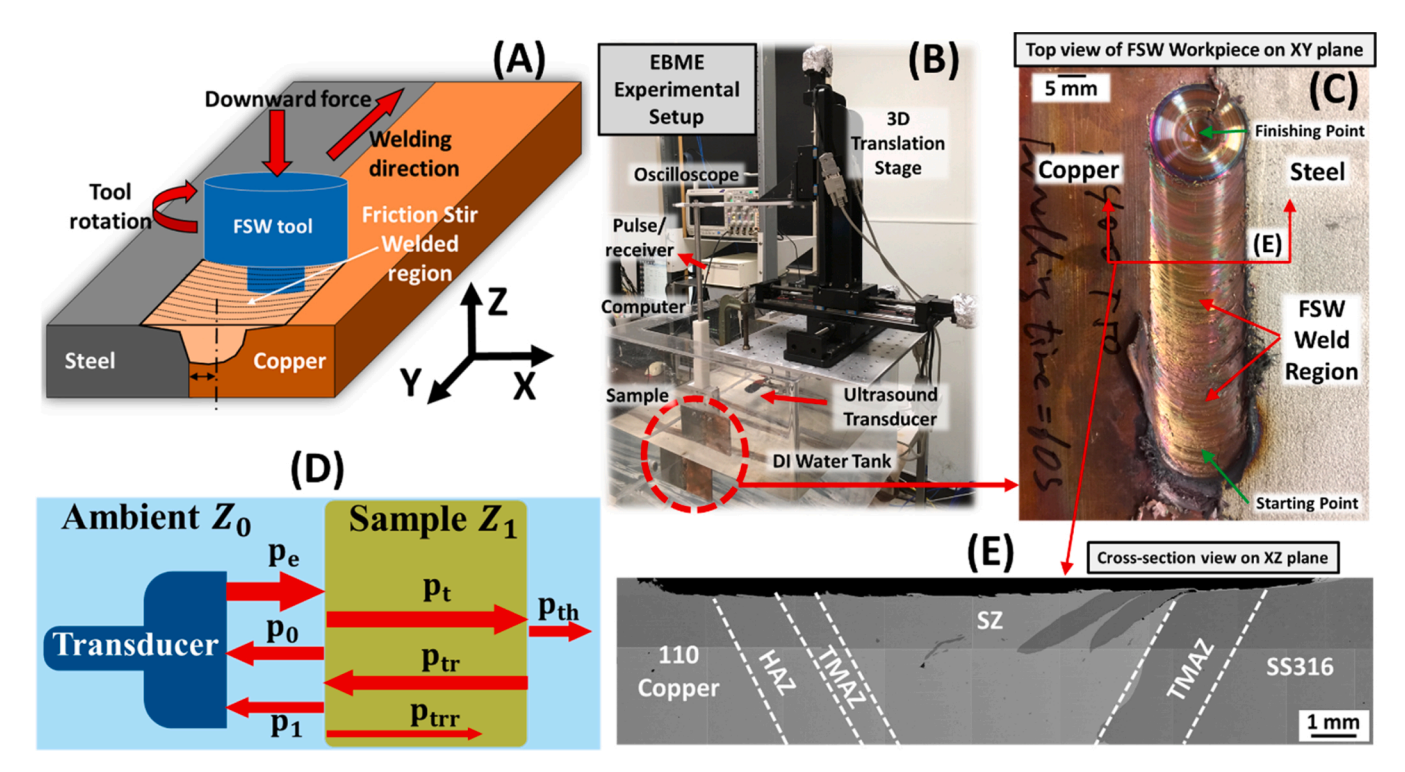


Fig. 1. (A) Illustration of FSW process on the Cu/SS316 workpiece. (B) The EBME setup. (C) Copper and stainless steel 316 FSW joint. (D) Schematic configuration of acoustic signals emitted by the source and then transmitted, reflected, and detected as the second echo. The illustration is not according to real scale. (E) Scanning electron microscopy of a cross-section of Cu/SS 316 FSW workpiece. HAZ: Heat affected zone. TMAZ: Thermo-mechanical affected zone. SZ: Stir zone.

EBME measurement of the bulk modulus as our previous work showed in Jin et al. (2019). At each measurement, the acoustic beam interacts with a material cylinder of the volume $V_{eff} = \pi \left(\frac{W_{FWFIM}}{2}\right)^2 t$, where t is the sample thickness and W_{FWHM} is the width of the acoustic beam at FWHM. The measured dynamic elastic modulus is the result of self-averaging over this volume as the existing study showed by Szabo and Lewin (2013). At the next step of acoustic scanning, the averaging occurs over the volume, which partially overlaps with the previous one. The non-overlapping parts of two neighboring volumes contribute a difference to the measurement that results in a smooth, position-dependent elastic bulk modulus.

3. Results and discussion

Fig. 2 shows the variation of the dynamic bulk modulus along 35 mm of the lateral axis and 8 mm of the welding axis estimated from the ultrasonic scanning over the cross-section encompassing the dissimilar metal joints. This area also included the stir zone (SZ) on either side of the metal joint. The initial point of the welding process located at 0 mm on the welding axis was not scanned in these measurements. Fig. 1(C) shows that the edge of the copper workpiece located from -20 mm to -15 mm was unaffected by the welding process. In Fig. 2, a sizeable heat-affected zone (HAZ) was observed in copper from -15 mm to -7.5 mm on the lateral axis due to an apparent reduction due to thermal softening during the welding process. The thermo-mechanically affected zone (TMAZ) was about 3 mm wide and occurs beside the SZ, which exhibits a strengthening effect. In the welded path region (SZ), another dynamic bulk modulus valley floor was distinctly observed near the welded interface.

On the other hand, a peak modulus was observed in steel next to the welded interface. It is assumed to occur from the mismatch of thermal expansion during welding and thermal contraction after welding. Specifically, linear thermal expansion coefficients of copper and steel are around $17\times10^{-6}~\rm K^{-1}$ and $12\times10^{-6}~\rm K^{-1}$, respectively. During friction stir welding, heat-induced expansion of copper in SZ is more significant than steel next to copper in SZ. After welding, the welded part cooled down to room temperature, and the thermal contraction happened on both copper and steel. Therefore, tensile residual stress remained in copper next to the welded interface, while residual compressive stress remained in steel next to the welded interface. The residual stress distribution

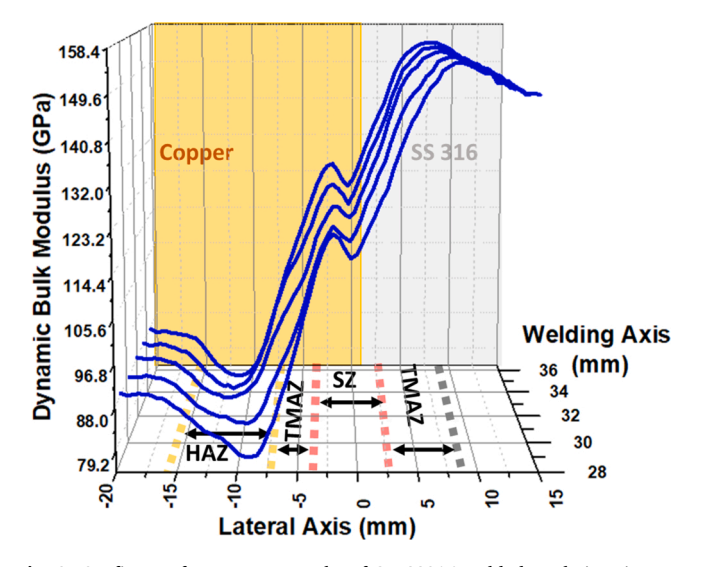


Fig. 2. 3D figure of raster scan results of Cu/SS316 welded workpiece in term of dynamic bulk modulus (z axis in figure) normalized to base copper value in a 35 mm (lateral axis, x) by 8 mm (welding axis, y) area. Unexpected effective bulk modulus drop was clearly showed around 1 mm in stir zone (SZ) region.

along the welded interface might be the reason for the unique dynamic bulk modulus distribution at the welded interface. Further investigation regarding the effect of residual stress on dynamic modulus is being conducted.

Additionally, during welding, SZ underwent a strong thermal softening once the temperature approached the copper's softening transition point. After the welding tool passed through, copper's recrystallization occurred in the SZ, which led to a weak strengthening effect. Along the welding axis, the averaged dynamic bulk modulus reduction in SZ is about 6%. Since cupper and stainless steel were immiscible, we expect no materials mixing composition variance happened during the welding process in SZ.

The effects of the welding process on each region examined by EBME was correlated with microhardness tests using two samples from the welded area. The samples from the center of the welding path were considered at around 30 mm on the welding axis (Fig. 2). As Fig. 3 (A) shows, the microhardness samples were selected from 1 mm and 2 mm depths, respectively. In Fig. 3(B), the hardness value of 1 mm and 2 mm depth samples are illustrated in red and blue lines. It can be observed that the high hardness in the stir zone (when Y = -1 mm) occurs due to the existence of steel fragments in the stir zone. Although microhardness represents localized plasticity, its behavior still shows strong agreement with elasticity (Fig. 2). From the microhardness test, the copper side HAZ was determined around 5 mm wide. The Cu side TMAZ was about 2.5 mm between HAZ and S.Z. In the SZ, from the sample hardness curve at 1 mm depth, an unexpected hardness deduction (Fig. 3(B), red line) occurs, aligned well with EBME results shown in Fig. 2.

In Fig. 2, the welding axis is from a point that is closer to the start of the stirring path to the point that is closer to the finishing point of the stirring path. Based on the EBME testing results, different lateral elasticity behaviors were discovered along the welding axis that is challenging to obtain by conventional test methods. Moreover, the weld axis's elasticity behavior has never been nondestructively mapped or reported in any prior reports. At the starting point, the rotating tool stirred much longer than the stirring path's middle region. The extra

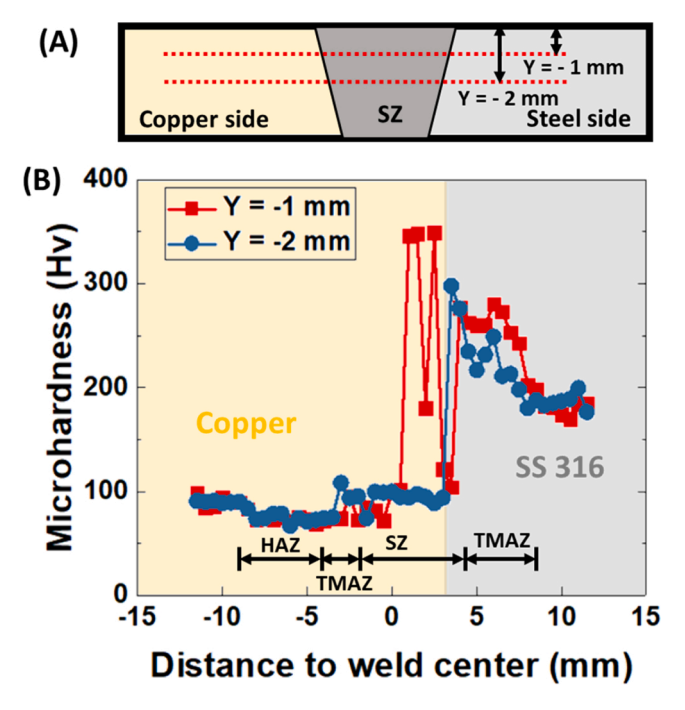


Fig. 3. Microhardness test of the Cu/SS 316 product which was tested by EBME in Fig. 2. The sample was occurred from the middle position on the welding path (about 31 mm at welding axis in Fig. 2). **(A)** Demonstration of the depth of two microhardness curve occurred. **(B)** Microhardness test results of 1 mm depth and 2 mm depth.

amount of heat leads to a different lateral elasticity behavior along the welding axis and results in a larger area and weaker elastic modulus in the HAZ. In Fig. 2, a clear large HAZ was observed on the copper side from 28 mm to 30 mm along the welding axis with the width from around 10 mm to 3 mm.

The dynamic bulk modulus values were significantly lower in the region closer to the initial point of the welding process due to a more extended stirring period. This reduction is because of the friction stir welding process, which can be divided into plunging and traversing. The plunging stage generally occurs for several seconds, and some dwell time after plunging is also applied to establish a steady thermal field before the welding tool starts to traverse. Therefore, excessive friction heat is always observed during the plunge stage of friction stir welding. The non-uniform heat effect was also illustrated in the SZ of this workpiece. The dynamic bulk modulus values were lower at the locations closer to the starting point of the welded path. Metallurgically, the thermal softening impact was significantly greater than the thermalmechanical strengthening effect from stirring due to excessive friction heat from the initial point of the welding process. In industries, the beginning and ending regions of the FSW workpiece were usually cut and waived around 15-30 mm long on the welding axis based on technical experience. Using this fast and non-invasive EBME technique, each workpiece could be individually evaluated to find a reasonable region size that can be discarded to avoid waste of material and use a higher quality of the joined materials involved in the finished products.

The mechanical properties of FSW products are highly dependent on welding parameters studied by Cavaliere et al. (2006) and Cavaliere et al. (2008), as well as tool features reported by Badarinarayan et al. (2009); Fujii et al. (2006) and Jata et al. (2000). Rai et al. (2011) reported that tool wear introduces significant instability of FSW product quality, which might lead to distinct variations between pieces fabricated in the production line which has been verified by Fall et al. (2016) and Tarasov et al. (2014). EBME can provide a fast and nondestructive evaluation of the products. As compared with local evaluation of microscale mechanical properties, the dynamic bulk modulus reveals an effective measure of the elastic modulus over a broader cross-section, which is preferable for industrial and practical applications.

Besides the formation of brittle reaction products, stress concentration is the primary factor for failure at dissimilar joints' welded interface. Assuming a uniformly distributed load is applied to the product, the stress concentrates on the mismatched elasticity region, and larger deformation/elongation could be obtained in the lower elastic modulus region. The initial stress and elongation developed at the weak zone under the influence of a time-independent external force are within the linear elastic limit of deformation instead of the plasticity regime. In the case of destructive testing, the deformation force can be large enough to induce initial stress and local deformation increase at the interface of dissimilar metals that extend beyond the linear regime.

On FSW products, failure could be predicted based on the continuous elastic modulus map from EBME testing as the high-frequency perturbating force due to the ultrasonic waves. When stress concentrates around the lowest elastic modulus region on a workpiece, the most extensive deformation/elongation would be located near the point at which the failure initializes. From the Cu and SS316 workpiece, as our recently study Wang and Mishra (2019) reported that the failure crack initiation and propagation on the products is located at the low elastic modulus side in mismatched elasticity region during mechanical tests. EBME testing result in Fig. 2 exhibits two highly elasticity mismatched regions. One is located between HAZ and TMAZ at the copper side. Another elasticity mismatched dynamic bulk modulus region is located around ~1 mm to the left side of the interface between Cu and SS316. Around 32-33 mm along the welding axis, the elastic modulus reaches a local minimum on the Copper HAZ. The reduction of elastic modulus here is close to the reduction observed in the SZ.

Hence, we introduce the elasticity mismatch factor dK/dx to predict the region would have more stress concentrated in the tensile test. As

illustrated in Fig. 4, the elasticity mismatch factor in SZ mismatched region (Zone 2) is 20.8 % higher than the Cu side HAZ/TMAZ mismatched region (Zone 1). Therefore, significantly more stress would concentrate in Zone 2, leading to a large deformation in the practical use and mechanical test of this cross-section.

In Fig. 5, the cross-section sample was cut from the Cu/SS316 workpiece in the location around 32 mm on the welding axis in Fig. 2(A) and (B) to do a digital image correlation analysis monitoring the tensile test. The tensile test result shows that a crack was initiated and propagated along the predicted location observed from the EBME result. Within the linear elastic region (stage 1 in the upper panel of Fig. 5(B)) we report larger elongation on the base copper side, that agrees with our EBME results. Once the elongation exceeds the linear stage and reaches the plastic elongation region (stage 2, middle panel), strain is concentrated at the elasticity mismatched location (see the right lower corner in the SZ). Such significant plastic elongation eventually results in initiation of a crack.

The EBME technique provides a continuous elastic modulus map. It is aided by much more precise numerical analysis on each product to provide useful information about the joint's mechanical strength for optimizing its application. The product's dynamic bulk modulus map could be input to finite element analysis to simulate the stress and deformation distribution by the conditions from its application. A tensile stress measurement can be combined with the above experiments to extract Young's modulus of the material at the interface.

EBME technique yields dynamic bulk modulus, which exhibits a maximum of 10 % difference between the TMAZ and HAZ in copper. This difference can be attributed to two factors. Firstly, the grain size in HAZ of copper is $\sim 15 \,\mu\text{m}$, while the grain size in base SZ, TMAZ, is ~ 10 μm, as shown in the Supplementary material (S1). HAZ represents the regions where the microstructure is influenced by heat only, which leads to grain growth. In contrast, TMAZ represents the regions where the microstructure is influenced by both heat and mechanical stress. Besides, TMAZ is always located between SZ and HAZ. Grains in HAZ of copper side tend to grow due to heat effect during friction stir welding. Various simulations to predict the grain size evolution during friction stir welding were reported by Fratini et al. (2009) and Heidarzadeh et al. (2015). The dynamic modulus variation between the property zones (HAZ, TMAZ, and SZ) is contributed by the acoustic Rayleigh scattering and its attenuation, as the existing study stated firstly by Papadakis (1963) and verified by Wan et al. (2017) recently. At the measured locations, the averaged grain size along the thickness is inverse proportional to measured dynamic bulk modulus, i.e., larger grain size usually means softer medium. This factor becomes less critical if the wavelength increases since the medium become more homogeneous, resulting in weaker attenuation. The detailed mechanism stated in the Supplementary material Section 1.

Secondly, residual stress distribution in the workpiece can influence sound speed [26], thus affecting the measured dynamic bulk modulus. Note that residual stress at HAZ of FSW product tends to be in tensile residual stress, while SZ/TMAZ/base next to HAZ tends to be compressive residual stress or tensile residual stress but lower than that in HAZ which has been thoroughly studied by Aval (2015) and Prime et al. (2006). In this study, no frequency dispersion effects demenstrated by Jin et al. (2020a) was observed in wave propagation in this Cu/SS316 workpiece. This was confirmed from the frequency-dependent speed of sound tests presented in the Supplementary material (S1). Besides the FSW copper and SS316 joint, we have also tested miscible dissimilar materials, namely, FSW Copper 110 and AZ31 and magnesium alloy with aluminum and zinc joint, See Supplementary material (Section 3). In the case of similar alloys or the same material welding, the EBME curves exhibit HAZ and TMAZ on both sides of the base materials.

The results obtained from EBME give the averaged over the sample depth (thickness) dynamic bulk modulus distribution on the raster scanned plane (horizontal plane in this study). The proposed technique cannot directly locate the exact position of a void in the welded work-

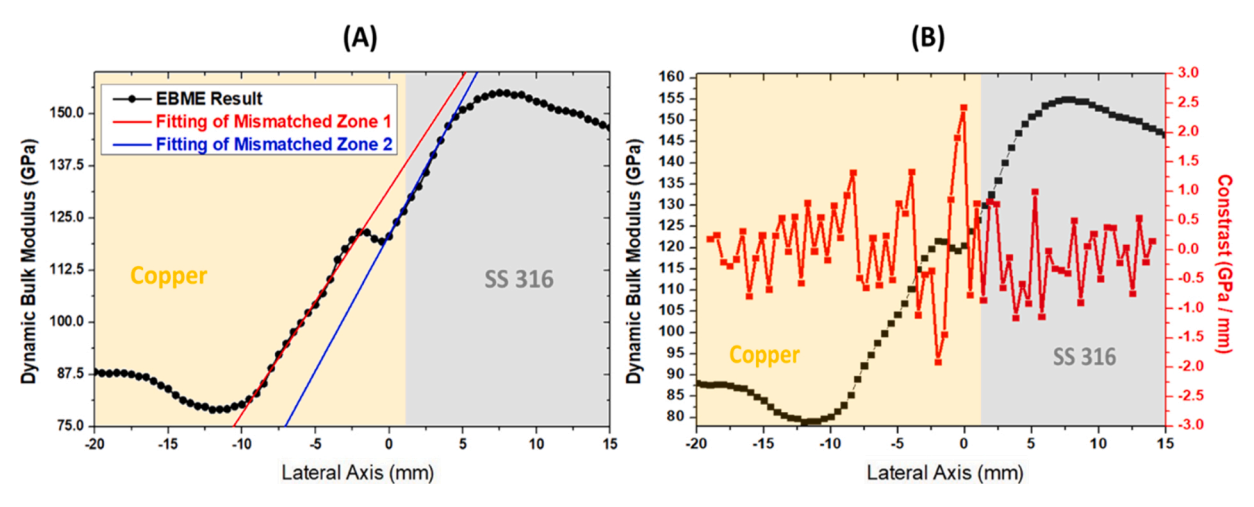


Fig. 4. (A) Linear curve fitting of the two elasticity mismatched zones. Black dot solid line is the dynamic bulk modulus of a cross-section sample from 32 mm on welding axis (Fig. 2). Red (Blue) solid line is the fitted line describing the elasticity mismatch factor dK/dx = 5.39 (6.51) in first (second) mismatched zone. **(B)** Red line is the point by point elasticity contrast calculated as dK/dx (in GPa/mm), which referred to a maximum elasticity mismatched point located around 0 mm on lateral axis.

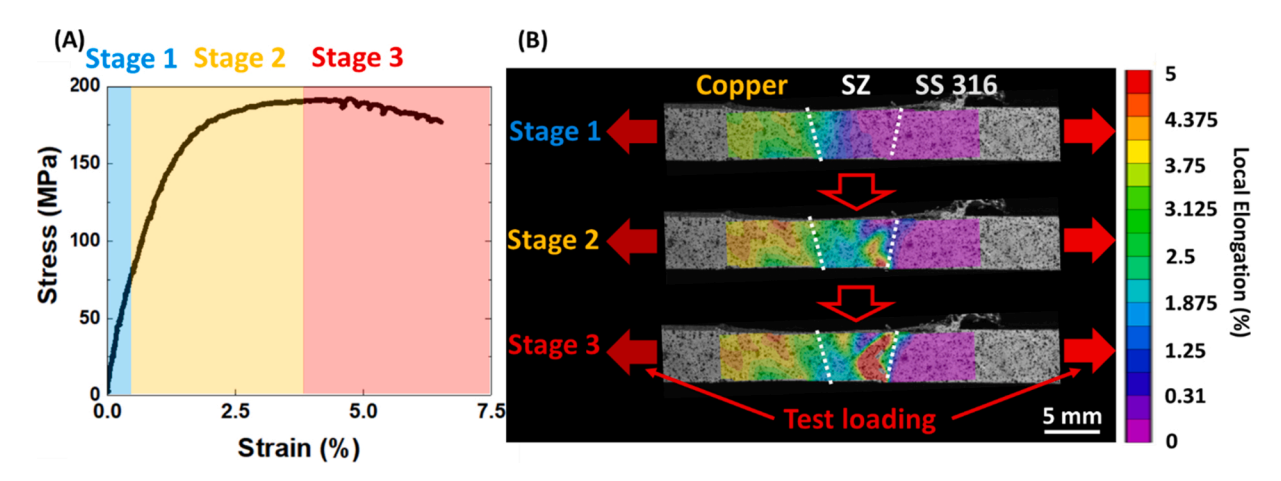


Fig. 5. (A) Stress strain relation from digital imaging processed tensile test. (B) was digital imaging processed tensile test of the cross-section sample. The color bar illustrated the local elongation from 0 to 5%. The sample was occurred from the middle position on the welding path (about 32 mm at welding axis in Fig. 2). Stage 1 indicated the linear elastic deformation on the sample. Stage 2 showed the stress was concentrated on the right of SZ due to highly mismatched elasticity. In the mismatched region the modulus of elasticity has reduced value, leading to larger deformation. This eventually becomes a source of a developing crack. Stage 3 showed the crack propagation along the elasticity dropped region in SZ.

pieces. However, a drop in the distribution of the dynamic bulk modulus $K=c^2~\rho_{eff}$ serves as an indication of possible presence of a void in the region with reduced effective density ρ_{eff} . The experimental setup requires a high-precision alignment of the transducer plane and the sample's surface for accurate measurement of the dynamic bulk modulus measurement. An error in the transducer's orientation, leading to a slightly oblique angle of incidence, can result in overestimated values for the dynamic elastic modulus. The samples were scanned from the front (rough) or back (smooth) side. For the Cu/SS316 workpiece, both orientations give very similar results. The results obtained for the Cu/AZ31 workpiece exhibit essential difference: scanning from the front (rough) surface gives lower values for the dynamic bulk modulus in the stir zone as compared with the values obtained for scanning from the back (smooth) side (see Supplementary material Section 4).

4. Conclusion

A recently developed non-invasive ultrasonic elastomapping technique was applied on friction stir welded metallurgically immiscible copper-steel structure in the current study. The regions such as base

material, heat-affected zone, and thermo-mechanical affected zone were clearly illustrated in the elasticity distribution map. From the elasticity mismatch map, the spatial location of the crack's initiation around the joint was accurately predicted nondestructively and corroborated by tensile tests and digital image correlation analysis. The technique successfully correlated the elasticity mismatch with crack initiation using a dynamic bulk modulus distribution map beside the existence of brittle intermetallic compound in miscible dissimilar materials joint.

In summary, there are two main advantages of the present technique. First, this technique can obtain the elasticity distribution of dissimilar joint nondestructively without any sample preparation. Consequently, the evaluation of the mechanical process using this technique is much faster than conventional measurement methods. Furthermore, the present technique can be applied for various welded structures to detect any unexpected elastic modulus drop, which can become a hazardous location while the structure is under mechanical stress.

Author contributions

Conceptualization, A.N., and R.M.; methodology, Y.J., and T.W.;

writing—original draft preparation, Y.J., T.W., T.-Y.C., A.K.; writing—review and editing, A.K., Y.J., A.N., T.W. and R.M; supervision, A. N.; project administration, R.M., A.N.; funding acquisition, A.N. All authors have read and agreed to the published version of the manuscript.

CRediT authorship contribution statement

Yuqi Jin: Methodology, Investigation, Software development, Conceptualization, Validation. Tianhao Wang: Sample preparation, Data Analysis, Validation; Arkadii Krokhin: Data curation, modeling, writing, reviewing and editing; Tae-Youl Choi: reviewing and editing. Rajiv Mishra: Reviewing and editing. Arup Neogi: Conceptualization, Data Analysis, Supervision, Writing- Original draft preparation.

Declaration of Competing Interest

The authors report no declarations of interest.

Acknowledgments

This work is supported by an Emerging Frontiers in Research and Innovation grant from the National Science Foundation (Grant No. 1741677) and Advanced Materials and Manufacturing Processes Institute (AMMPI) 2019 SEED grants. The authors also acknowledge the infrastructure and support of the Center for Agile & Adaptive and Additive Manufacturing (CAAAM) funded through the State of Texas Appropriation (#190405-105-805008-220).

Appendix A. Supplementary data

Supplementary material related to this article can be found, in the online version, at doi:https://doi.org/10.1016/j.jmatprotec.2021. 117301.

References

- Akella, S., Harinadh, V., Krishna, Y., Buddu, R.K., 2014. A welding simulation of dissimilar materials SS304 and copper. Procedia Mater. Sci. 5, 2440–2449.
- Aval, H.J., 2015. Microstructure and residual stress distributions in friction stir welding of dissimilar aluminium alloys. Mater. Des. 87, 405–413.
- Badarinarayan, H., Yang, Q., Zhu, S., 2009. Effect of tool geometry on static strength of friction stir spot-welded aluminum alloy. Int. J. Mach. Tools Manuf. 49, 142–148.
- Cavaliere, P., Campanile, G., Panella, F., Squillace, A., 2006. Effect of welding parameters on mechanical and microstructural properties of AA6056 joints produced by friction stir welding. J. Mater. Process. Technol. 180, 263–270.
- Cavaliere, P., Squillace, A., Panella, F., 2008. Effect of welding parameters on mechanical and microstructural properties of AA6082 joints produced by friction stir welding. J. Mater. Process. Technol. 200, 364–372.
- Coelho, R., Kostka, A., Dos Santos, J., Pyzalla, A., 2008. EBSD technique visualization of material flow in aluminum to steel friction-stir dissimilar welding. Adv. Eng. Mater. 10, 1127–1133.
- DebRoy, T., Bhadeshia, H.K.D.H., 2010. Friction stir welding of dissimilar alloys—a perspective. Sci. Technol. Weld. Join. 15, 266–270.
- Du, Y., Mukherjee, T., DebRoy, T., 2019. Conditions for void formation in friction stir welding from machine learning. NPJ Comput. Mater. 5, 1–8.
- Du, Y., Mukherjee, T., Mitra, P., DebRoy, T., 2020. Machine learning based hierarchy of causative variables for tool failure in friction stir welding. Acta Mater. 192, 67–77.
- Fall, A., Fesharaki, M.H., Khodabandeh, A.R., Jahazi, M., 2016. Tool wear characteristics and effect on microstructure in Ti-6Al-4V friction stir welded joints. Metals 6, 275. Fratini, L., Buffa, G., Palmeri, D., 2009. Using a neural network for predicting the average
- grain size in friction stir welding processes. Comput. Struct. 87, 1166–1174. Fujii, H., Cui, L., Maeda, M., Nogi, K., 2006. Effect of tool shape on mechanical properties
- and microstructure of friction stir welded aluminum alloys. Mater. Sci. Eng. A 419, 25–31.

 Hartl, R., Landgraf, J., Spahl, J., Bachmann, A., Zaeh, M.F., 2019. Automated visual
- Hartl, R., Landgraf, J., Spahl, J., Bachmann, A., Zaeh, M.F., 2019. Automated visual inspection of friction stir welds: a deep learning approach. Multimodal Sens. Technol. Appl. 11059, 1105909.
- He, J., Chen, Z., Luo, X., 2020. A Bayesian estimation-based uncertainty quantification of flaws in steel welds detected by ultrasound phased array. J. Phys. Conf. Ser. 1592, 012011.
- Heidarzadeh, A., Jabbari, M., Esmaily, M., 2015. Prediction of grain size and mechanical properties in friction stir welded pure copper joints using a thermal model. Int. J. Adv. Manuf. Technol. 77, 1819–1829.

- Heo, H., Jin, Y., Yang, D., Wier, C., Minard, A., Dahotre, N.B., Neogi, A., 2021. Manufacturing and characterization of hybrid bulk voxelated biomaterials printed by digital anatomy 3D printing. Polymers 13, 123.
- Jata, K.V., Sankaran, K.K., Ruschau, J.J., 2000. Friction-stir welding effects on microstructure and fatigue of aluminum alloy 7050-T7451. Metall. Mater. Trans. A 31, 2181–2192.
- Jin, Y., Walker, E., Krokhin, A., Heo, H., Choi, T.-Y., Neogi, A., 2019. Enhanced instantaneous elastography in tissues and hard materials using bulk modulus and density determined without externally applied material deformation. IEEE Trans. Ultrason. Ferroelectr. Freq. Control 67, 624–634.
- Jin, Y., Heo, H., Walker, E., Krokhin, A., Choi, T.Y., Neogi, A., 2020a. The effects of temperature and frequency dispersion on sound speed in bulk poly (Vinyl Alcohol) poly (N-isopropylacrylamide) hydrogels caused by the phase transition. Ultrasonics 104, 105931.
- Jin, Y., Walker, E., Heo, H., Krokhin, A., Choi, T.Y., Neogi, A., 2020b. Nondestructive ultrasonic evaluation of fused deposition modeling based additively manufactured 3D-printed structures. Smart Mater. Struct. 29, 045020.
- Jin, Y., Yang, T., Heo, H., Krokhin, A., Shi, S.Q., Dahotre, N., Choi, T.-Y., Neogi, A., 2020c. Novel 2D dynamic elasticity maps for inspection of anisotropic properties in fused deposition modeling objects. Polymers 12, 1966.
- Lévesque, D., Asaumi, Y., Lord, M., Bescond, C., Hatanaka, H., Tagami, M., Monchalin, J.-P., 2016. Inspection of thick welded joints using laser-ultrasonic SAFT. Ultrasonics 69, 236–242.
- Lienert, T.J., Stellwag Jr., W.L., Grimmett, B.B., Warke, R.W., 2003. Friction stir welding studies on mild steel. Weld. J. New York 82, 1–5.
- Mai, T.A., Spowage, A.C., 2004. Characterisation of dissimilar joints in laser welding of steel-kovar, copper-steel and copper-aluminium. Mater. Sci. Eng. A 374, 224–233.
- Mishra, D., Gupta, A., Raj, P., Kumar, A., Anwer, S., Pal, S., Chakravarty, D., et al., 2020. Real time monitoring and control of friction stir welding process using multiple sensors. CIRP J. Manuf. Sci. Technol. 30, 1–11.
- Pantawane, M.V., Yang, T., Jin, Y., Joshi, S.S., Dasari, S., Sharma, A., Krokhin, A., et al., 2021. Crystallographic texture dependent bulk anisotropic elastic response of additively manufactured Ti6Al4V. Sci. Rep. 11, 1–10.
- Papadakis, E.P., 1963. Rayleigh and stochastic scattering of ultrasonic waves in steel. J. Appl. Phys. 34, 265–269.
- Peng, L., Yajiang, L., Juan, W., Jishi, G., 2003. Vacuum brazing technology and microstructure near the interface of Al/18-8 stainless steel. Mater. Res. Bull. 38, 1493–1499.
- Prime, M.B., Gnäupel-Herold, T., Baumann, J.A., Lederich, R.J., Bowden, D.M., Sebring, R.J., 2006. Residual stress measurements in a thick, dissimilar aluminum alloy friction stir weld. Acta Mater. 54, 4013–4021.
- Rai, R., De, A., Bhadeshia, H.K.D.H., DebRoy, T., 2011. Friction stir welding tools. Sci. Technol. Weld. Join. 16, 325–342.
- Shiraishi, D., Kato, R., Endoh, H., Hoshimiya, T., 2010. Destructive inspection of weld defect and its nondestructive evaluation by photoacoustic microscopy. Jpn. J. Appl. Phys. 49, 07HB13.
- Sudhagar, S., Sakthivel, M., Ganeshkumar, P., 2019. Monitoring of friction stir welding based on vision system coupled with Machine learning algorithm. Measurement 144, 135–143.
- Szabo, T.L., Lewin, P.A., 2013. Ultrasound transducer selection in clinical imaging practice. J. Ultrasound Med. 32, 573–582.
- Taban, E., Gould, J., Lippold, J., 2010. Dissimilar friction welding of 6061-T6 aluminum and AISI 1018 steel: properties and microstructural characterization. Mater. Des. 31, 2305–2311.
- Tanaka, T., Morishige, T., Hirata, T., 2009. Comprehensive analysis of joint strength for dissimilar friction stir welds of mild steel to aluminum alloys. Scr. Mater. 61, 756–759.
- Tarasov, S.Y., Rubtsov, V.E., Kolubaev, E.A., 2014. The effect of friction stir welding tool wear on the weld quality of aluminum alloy AMg5M. AIP Conf. Proc. 1623, 635–638.
- Thomas, W.M., Nicholas, E.D., J. C, N., Church, M., Templesmith, P., Dawes, C., 1991. Friction Stir Butt Welding, International Patent.
- Thomas, W.M., Threadgill, P.L., Nicholas, E.D., 1999. Feasibility of friction stir welding steel. Technol. Weld. Join. 4, 365–372.
- Tsujino, J., Hidai, H., Hasegawa, A., Kanai, R., Matsuura, H., Matsushima, K., Ueoka, T., 2002. Ultrasonic butt welding of aluminum, aluminum alloy and stainless steel plate specimens. Ultrasonics 40, 371–374.
- Uzun, H., Dalle Donne, C., Argagnotto, A., Ghidini, T., Gambaro, C., 2005. Friction stir welding of dissimilar Al 6013-T4 to X5CrNi18-10 stainless steel. Mater. Des. 26, 41-46.
- Venkatakrishna, A., Lakshminarayanan, A.K., Menaka, M., 2020. Monitoring the quality of friction stir welded joints by infrared thermography. In: Analysis of Tensile Deformation Behavior in Friction Stir Welded P91-316LN Dissimilar Joints Using Infrared Thermography, Vol. 979, pp. 114–118.
- Wan, T., Naoe, T., Wakui, T., Futakawa, M., Obayashi, H., Sasa, T., 2017. Effects of grain size on ultrasonic attenuation in type 316L stainless steel. Materials 10, 753.
- Wang, T., Mishra, R., 2019. Effect of Stress Concentration on Strength and Fracture Behavior of Dissimilar Metal Joints. Friction Stir Welding and Processing X, pp. 33–39.
- Wang, T., Shukla, S., Nene, S.S., Frank, M., Wheeler, R.W., Mishra, R.S., 2018. Towards obtaining sound butt joint between metallurgically immiscible pure Cu and stainless steel through friction stir welding. Metall. Mater. Trans. A 49, 2578–2582.
- Wu, Yan, Siqun, W., Dingguo, Z., Cheng, X., Yang, Z., Zhiyong, C., 2010. Evaluation of elastic modulus and hardness of crop stalks cell walls by nano-indentation. Bioresour. Technol. 101, 867–2871.

- Xue, P., Ni, D.R., Wang, D., Xiao, B.L., Ma, Z.Y., 2011. Effect of friction stir welding parameters on the microstructure and mechanical properties of the dissimilar Al–Cu ioints. Mater. Sci. Eng. A 528, 4683–4689.
- Yao, C., Xu, B., Zhang, X., Huang, J., Fu, J., Wu, Y., 2009. Interface microstructure and mechanical properties of laser welding copper–steel dissimilar joint. Opt. Lasers Eng. 7–8, 807–814.
- Zuev, L.B., Poletika, I.M., Semukhin, B.S., Bushmelyova, K.I., Kulikova, O.A., 1999. The ultrasound velocity and mechanical properties of metals and alloys. Metall-Heidelberg 53, 490–492.